ESRF	**Experiment title:** Exploring the local and mesoscopic structure of $Ce_{1-x}Gd_xO_{2-x/2}$ nanoparticles by means of Pair Distribution Function and Debye Function Analyses	**Experiment number**: CH-5157
Beamline: ID22	**Date of experiment**: from: 31/01/2018 to: 06/02/2018	**Date of report**: 02/03/2018
Shifts: 18	**Local contact(s)**: CODURI Mauro	*Received at ESRF:*

Names and affiliations of applicants (* indicates experimentalists):

Marco Scavini*[,1], Federica Bertolotti*[,2,3], Antonietta Guagliardi*[,4], Mauro Coduri*[,5], Stefano Checchia[5], Jonadri Mlloja*[,1], Mariangela Longhi*[,1,] Masciocchi Norberto[3]

[1]Università degli Studi di Milano, Dip. di Chimica, Milano, Italy [2]Aarhus University, Aarhus Institute of Advanced Study (AIAS), Aarhus, Denmark, [3] University of Insubria & To.Sca.Lab., Como, Italy, [4]CNR - Istituto di Cristallografia & To.Sca.Lab., Como, Italy; [5]ESRF,

Report:

Aim of the experiment was to unveil the local structure of $Ce_{1-x}Gd_xO_{2-x/2}$ (hereafter CGO) nanocrystals with variable composition and surface to bulk ratio by means of a jointed Pair Distribution Function (PDF) and Debye Function Analysis (DFA) investigation. Both techniques take advantage of total scattering approach supplying complementary information on the local and mesoscopic structure of CGO nano-crystals varying composition and crystallite size.

Brief Introduction to the scientific problem

Gadolinium doping of Cerium oxide induces fast ionic conductivity (σ_i), making CGO compounds suitable oxygen ion-conducting electrolytes for intermediate temperature electrochemical cells (~500-700 °C)[1] and, more in general, for applications were the oxygen diffusion rate plays a role. Nanostructuring strongly improves the above properties in respect to bulk materials; in fact, the crystal size is supposed to directly influence the way defects interact, by reason of the preferential segregation of dopants and oxygen vacancies at the grain boundaries.[2]

In a previous experiment performed at the High Resolution beamline of the ESRF on CGO solid solutions we showed that dopant ions and oxygen vacancies form large clusters with *Ia*-3 symmetry (the same of C-type Gd_2O_3) enclosed in a fluorite CeO_2-like matrix (*Fm*-3*m* symmetry).[3,4] By increasing *x*, clusters evolve into dopant-rich nanodomains spanning some tens of nanometers.[4]

PDF analysis supplies simple structural fingerprints to unveil the presence of dopant(s)-vacancies clusters.

As an example, at the very short range, in $Ce_{1-x}Gd_xO_{2-x/2}$ solid solutions with fluorite structure each metal ion (M=Ce, Gd) should be surrounded by (8-4x) oxygen ions (peak A of both PDF in Figure 1) as nearest neighbours and by 12 metal ions as next nearest neighbours, all at the same distance (~3.8 Å, peak B in the PDF at the left side of Figure 1). When defect clusters form, metal ions are pushed far away from oxygen ions resembling locally the C-type structure of Gd_2O_3[3,4]. The 12 M-M equal distances split into two sets of 6 shorter (~3.6 Å) and 6 longer (~4.1 Å) distances (peaks B and C PDF at the left side of Figure 1).

The presence of the C peak is a fingerprint of M relaxation around the oxygen vacancy and of defect clustering. In bulk material its intensity rises monotonically by increasing Gd concentration at least for x≥0.125 [3,4].

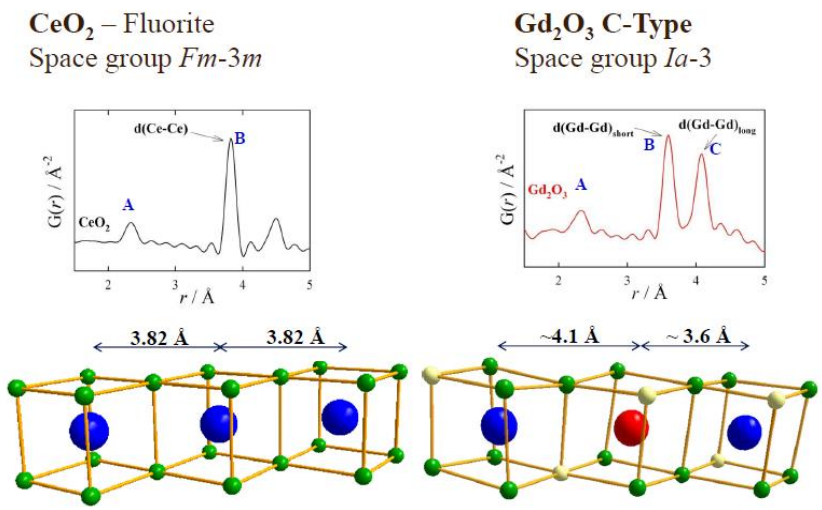

Figure 1.

Left: short range PDF of fluorite CeO_2 (top) and sketch of the local environment of Ce reporting the Ce-Ce NNN distances (bottom).

Right: short range PDF of C-type Gd_2O_3 (top) and sketch of the local environment of Gd reporting the Gd-Gd NNN distances (bottom).

Labels A, B, C are described in the text

Experimental details

CGO samples of about 2 nm in diameter were prepared using a reverse micellar wet synthetic path extending the work of Ref.(5) to CeO_2 and $Ce_{1-x}Gd_xO_{2-x/2}$ solid solutions. Samples in the compositional range $0 \leq x \leq 0.625$ were synthetized at room temperature. 0.24 M aqueous solutions with different Ce^{3+}/ Gd^{3+} ratios were prepared and dispersed in a mixture of n-octane, 1-butanol, and CTAB to form a micro-emulsion (ME). A second ME of similar composition was made using NaOH instead of Ce^{3+}/ Gd^{3+} salts. The two stable ME were then mixed and allowed to react for 2 hours at RT. Also the mixed ME is stable during the whole reaction time. Great care has been dedicated to keep identical experimental conditions in all the synthesis (ionic strength, temperature, reaction time et cetera). While optimizing the synthesis parameters we identified the Ce/Gd ratio and the ionic strength as key parameters to vary the nanoparticles size, structure, defectivity and properties

Samples were then dried/annealed at 200 °C for 4 hours. Aliquots of each batch were then annealed at 500 or 900 °C (additionally at 400 °C or 700 °C for selected samples) obtaining powder of increasing crystallite dimensions. EMPA analysis confirmed that the actual Ce/Gd ratios were very close to the nominal ones.

All XRPD measurements were carried out at the ID22 beamline of the ESRF. Three distinct sets of data were collected, each requiring appropriate experimental conditions:

1) DFA[6,7] quality measurements were carried out on samples in high resolution (HR) setup using the 9-channel Si 111 multianalyser stage, a wavelength λ=0.354351 Å and counting time of ~2 hour/measurement to reach the desired signal to noise ratio and a suitable Q_{max}(~12-15 $Å^{-1}$). Scattering signals from the empty capillary and sample environment were collected in the same experimental conditions, in order to be subtracted from the samples pattern. Absorption correction may be a critical step for DFA for highly absorbing nanopowders measured in transmission geometry; aiming at minimizing absorption effects, 0.5 mm capillaries were used (instead of 1.0 mm, as done in PDF measurements) and the linear absorption coefficient estimated for each sample by measuring the direct and transmitted beam intensities using a diode. Preliminary tests were also performed to record the (direct and transmitted) beam profile through a beam-viewer placed behind the sample; in this respect, a procedure for the automatic insertion of the devices and record of attenuation data during the sample-change will be implemented.
To our knowledge, this is the first DFA experiment at ID22@ESRF doing analytical absorption correction for strongly attenuating samples. For this reason, we spent a part of the experimental time to find the suitable collection strategy for DFA and to test the monitor.

2) PDF quality patterns on selected samples annealed at 700 °C and 900 °C ($D_V \geq 10$ nm) were collected using the same HR setup and 1.0 mm kapton capillaries (~5 hour/measurement, Q_{max}~27 $Å^{-1}$).

3) PDF quality patterns were collected on all the samples using the Perkin-Elmer 2D detector of ID22 beamline and a wavelength λ=0.177125 Å (~40 min/sample, Q_{max}~28.5 $Å^{-1}$). The focussing of the beam on the large 2D

detector allows obtaining a suitable *Q* resolution to observe ample PDF peaks up to interatomic distances as large as 20 nm in reference microcrystalline materials. This allowed avoiding the time consuming HR-PDF on nanomaterials (samples annealed at $T \leq 500$ °C).

Preliminary results on CGO size characterization

The accurate data analysis and rationalization is still in course because the experiment ended less than one month before the experimental report deadline. Despite this, some experimental evidences are below reported.

The Williamson-Hall (WH) analysis has been applied to the high resolution XRPD patterns in order to get a rude estimation of crystallite dimension D_V The results are presented in Figure 2a. DFA analysis provided accurate sizes and size distributions (according to a log-normal size function of spherical nanocrystals) for samples at T_{ann} = 400 and T_{ann} = 500°C, both series shown in Figure 2b; reasonable estimations are also obtained for samples at T_{ann} = 200 °C (also shown in Figure 2b). The results of WH and DFA methods are very well in agreement.
As expected, Figure 2 shows that the size of nanoparticles (NPs) depends on the annealing temperature that causes a coalescence of the NPs with an increase of their average sizes and size distributions.
Moreover, a clear dependence on the doping amount is also observed: the average diameter of the NPs progressively decreases while increasing the Gd amount, while their size distribution becomes narrower.
This trend is quite robust throughout the different syntheses of samples and compositions.
We underline that great care has been dedicated to keep identical experimental conditions in all the syntheses.
This suggests that size differences along the composition coordinate should be related to the mechanism of NPs nucleation and growth during the synthesis and successive sintering process during the annealing in a wide range of temperature values.

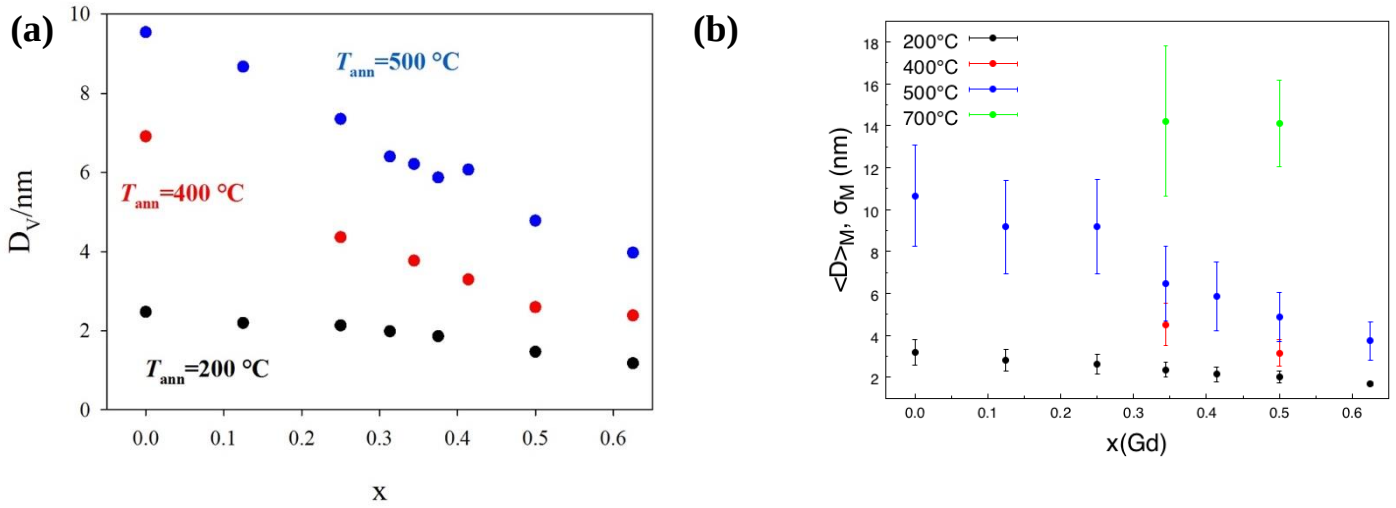

Figure 2. NPs sizes as a function of Gd doping amount, x, at different annealing T (Tann) values, determined through the WH and DFA analyses (a and b, respectively).

PDF analysis preliminary results.

In Figure 3 are reported the PDF curves of selected samples annealed at 200 °C. All PDF peaks broaden with increasing Gd concentration, probing that doping induces structural disorder.

However, the C peak at ~4.1 Å is absent in all the samples, even for Gd doping amount as large as x=0.50 where 1/8 of oxygen sites should be vacant. Thus, these PDFs show that the structural relaxation of metal ions away from the oxygen vacancy is frustrated and a very different defect architecture is present in in extremely small nanoparticles (D_v< 3 nm).

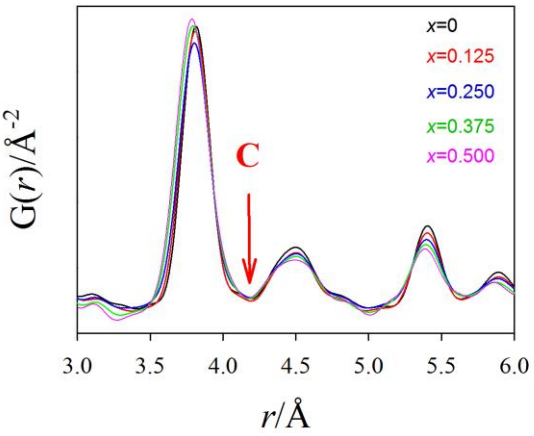

Figure 3

PDF of samples x=0, 0.125, 0.250, 0.375, 0.500 annealed at 200 °C
The arrow indicates the usual position of the **C** peaks, which is absent in these G(*r*).

Increasing the annealing *T* (T_{ann}) value, the coherence length of the crystallites increases as well, as an example, by the G(*r*) peaks amplitude for sample x=0.50 shown in Figure 4.

Focusing on the short range, the intensity of peak "C" at ~4.1 Å evolves with T_{ann}, as shown in the right side panels of Figure 4 for the cases of x=0.414 and 0.500. This feature, coupled to other G(*r*) peaks changes at larger *r* values testify that the defect architecture continuously evolves with the crystallite dimension. Data analysis is in progress.

Both WH and PDF analysis suggests that future work should deal with the investigation of the kinetics of NPs structural and morphological evolution during the synthesis and the successive annealing by means of in situ experiment(s).

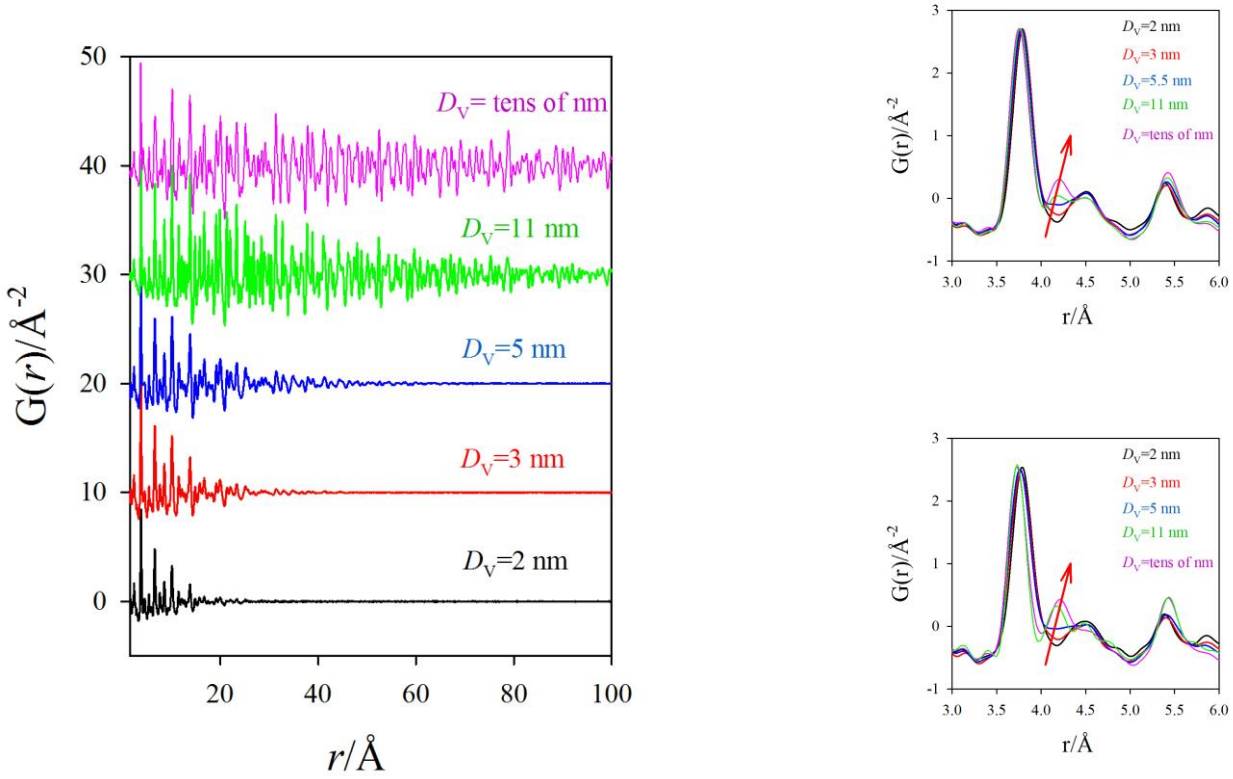

Figure 4. Left: PDF of *x* = 0.500 samples annealed at 200 (black), 400 (red), 500 (blue), 700 (green) and 900 (pink) °C. Right: Low r part of G(r) function of *x*=0.344 (top) and 0.500 (bottom) samples annealed at the same *T* values. Dv values are derived from DFA analysis (see Figure 2). The arrow indicates the position of the C peaks, whose intensity growth with the annealing temperature.

DFA preliminary results.

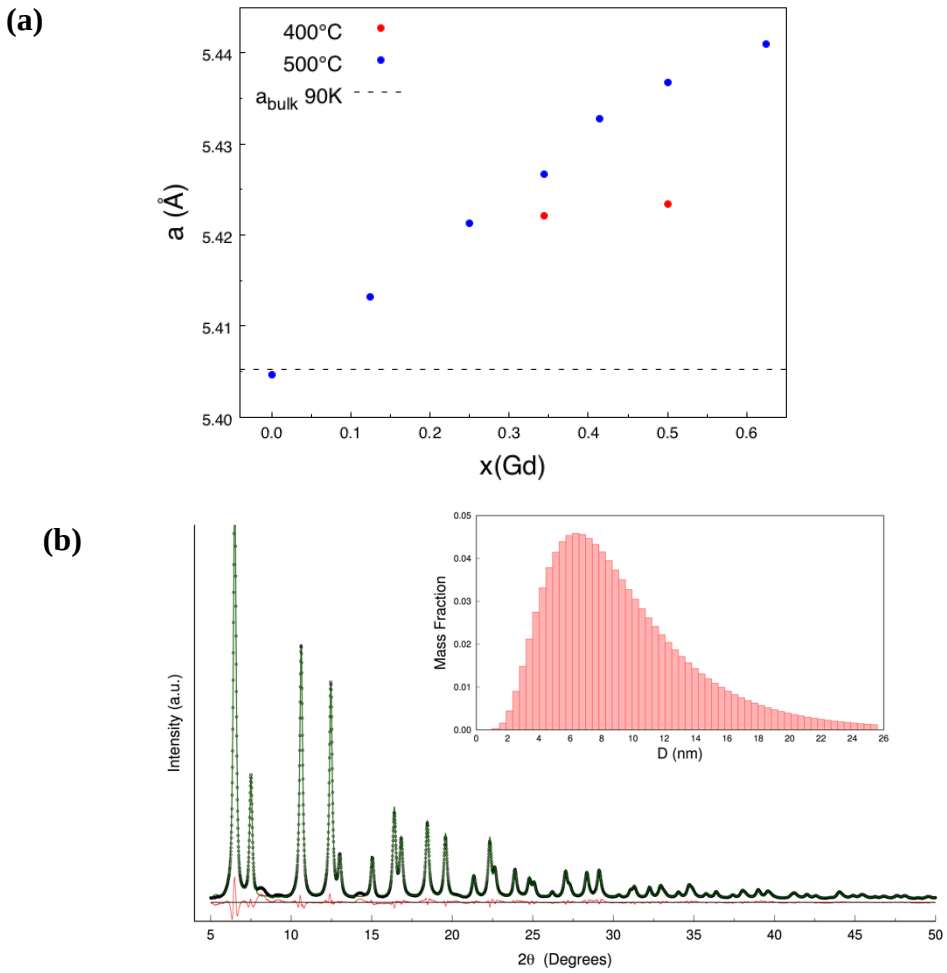

Figure 5. a) Average cell parameter of $Ce_{1-x}Gd_xO_{2-x/2}$ solid solutions versus Gd doping, x, at different temperatures of annealing (T_{ann}). **b)** Preliminary fit of the sample with x(Gd)=0.125 annealed at 500°C: the black points are the experimental data, the green line the simulated pattern, calculated using the Debye Scattering Equation. Inset: mass-based lognormal size distribution of the same sample refined through the DFA.

The dependence of the CeO_2 lattice parameter, *a*, upon increasing the Gd amount, is reported in Figure 5a. The increase of *a* vs Gd doping, already reported for the bulk material in ref. 3, is also found in the CGO series of NPs annealed at T_{ann}=500°C and (with a less pronounced effect) at T_{ann} = 400°C. When dealing with NPs, this effect can be due to a combination of both size and doping-induced cell expansion; however, by crossing size (Figure 2b) and lattice parameters (Figure 5a) of samples with the same doping (x=0.344 and x= 0.5) at different T_{ann}, a major influence of doping is suggested (larger *a* values are detected in larger NPs).

Figure 5a does not include the behaviour of sample at T_{ann} =200°C since, for each composition, a single unit cell parameter is not able to match the whole measured angular range; this finding suggests that surface effects (due to the very small size and/or Gd^{3+} inomogenous doping) and/or structural defects appear, which need further investigation. These effects become less important by rising T_{ann} and consequently the NPs sizes.

For T_{ann} = 700°C series the appereance of superstructure peaks, some of them compatible with the *C-type* Gd_2O_3 structure, suggests a more extended and complex clustering of the Gd subsitutions that must be further understood and determines a contraction of the unit cell parameters compared to the T_{ann} = 500°C series.

Summary and Future Work

We have investigated the structural and microstructural evolution of $Ce_{1-x}Gd_xO_{2-x/2}$ nanoparticles as a function of composition and annealing temperature by means of DFA and PDF analysis.
Both the defect architecture and the microstructure depend deeply on *x* and *T*. In particular, the metal relaxation around vacancies seems to be completely frustrated in small NPs (D_V<3 nm) while it progressively appears by increasing T_{ann} and D_V. These findings should be intimately related to the large improvement of nanoparticles oxygen diffusion coefficient in respect to bulk materials. The same NPs also show a more complex influence of Gd doping on the sample lattice parameter, suggesting inhomogeneous distribution within the NPs, as detected in the reciprocal space DFA characterization, that needs to be further investigated.
An accurate in-situ diffraction study during the nanoparticle nucleation, growth during the synthesis and successive annealing will help to rationalize the present findings and to suggest suitable reaction paths to obtain nanoparticles with higher performance and, possibly, retaining the low *T* defects architecture to the operational conditions (~500-700 °C for intermediate temperature electrochemical cells; lower *T* values for catalysts or electrocatalyst applications). Future work will face this problem.
This *in situ* study will require a fast data acquisition setup with a 2D detector, instead of a high-resolution setup, in order to ensure a good data statistic together with a satisfactory time resolution.
The requirement (especially for the DFA, for which all the extra sample scattering contributions needs to be avoided/corrected) of using a solid state detector with a very low intrinsic background will lead to a choice of a different ESRF beamline for these future experiments (e.g. ID15 instead of ID22).

Beside $Ce_{1-x}Gd_xO_{2-x/2}$, also Sm^{3+} and Y^{3+} doping of CeO_2 produce interesting (nano)materials for various applications such as sensors, oxygen separation membranes and catalysts. In our previous work on bulk materials we observed that the defect structure of $Ce_{1-x}Sm_xO_{2-x/2}$[8] and $Ce_{1-x}Y_xO_{2-x/2}$[9] is similar but not identical to CGO one. This brings to some different physical properties both in nanoparticles and bulk materials (e.g. oxygen diffusion coefficient values as a function of *T* and composition) which could be related to the different ionic radii of different dopants among them and in respect to Ce^{4+} ion.

For this reason, in a future experiment we would like to produce $Ce_{1-x}Sm_xO_{2-x/2}$ and $Ce_{1-x}Y_xO_{2-x/2}$ nanoparticle systems using the same wet synthetic path extending to them the experimental strategy described above as a function of composition and annealing temperature. Our experience on the $Ce_{1-x}Gd_xO_{2-x/2}$ system will help us to optimize the experimental procedure and select a smaller-but-significant set of samples.

References:

(1) Kilner, J. A. Chem. Letters, **2008**, *37*, 1012.

(2) Zhi-Peng Li, Toshiyuki Mori, Graeme John Auchterlonie, Jin Zou and John Drennan, **Appl. Phys. Lett**. 98, 093104 (2011)

(3) M. Scavini, M. Coduri, M. Allieta, M. Brunelli, C. Ferrero, **Chem. Mater.**, **24**, (2012) 1338.

(4) M. Scavini, M. Allieta, M. Coduri, P. Masala, M. Brunelli, S. Cappelli, C. Oliva, F. Orsini, C. Ferrero, **IUCrJ** 2 (2015) 511-522

(5) S. Sathyamurthy, K.J. Leonard, R.T. Dabestani, M.P. Paranthaman, **Nanotechnology** 16 (2005) 1960-64

(6) F. Bertolotti, D.N. Dirin, M. Ibáñez, F. Krumeich, A. Cervellino, R. Frison, O. Voznyy, E.H. Sargent, M.V. Kovalenko, A. Guagliardi, N. Masciocchi, **Nat. Mater**. **2016**, 15, 987-994

(7) A. Cervellino, R. Frison, F. Bertolotti, A. Guagliardi **J. Appl. Cryst.** (2015) 48, 2026-2032

(8) M. Coduri, P. Masala, M. Allieta, I. Peral, M. Brunelli, C. A. Biffi, . Scavini. **Inorganic Chemistry** 57(2) 2018 879–891.

(9) M. Coduri, M. Scavini, M. Brunelli, M. Allieta and C. Ferrero, **Chemistry of Materials 25** (2013) 4278-4289**.**